Discerning Rise Time Constants to Quantify Charge Carrier Extraction in Perovskite Solar Cells

Lennard Kruppa
  Forschungszentrum Jülich

Sandra Jenatsch
  Swiss Federal Laboratories for Materials Science and Technology

Yueming Wang
  Forschungszentrum Jülich

Sandheep Ravishankar (✉ s.ravi.shankar@fz-juelich.de)
  Forschungszentrum Jülich

Additional Declarations: There is **NO** Competing Interest.

Discerning Rise Time Constants to Quantify Charge Carrier Extraction in Perovskite Solar Cells

Sandheep Ravishankar,[1]* Lennard Kruppa[1], Sandra Jenatsch[2], Yueming Wang[1]

[1]IEK-5 Photovoltaik, Forschungszentrum Jülich, 52425 Jülich, Germany
[2]Fluxim AG, Katharina-Sulzer-Platz 2, 8406 Winterthur, Switzerland

*author for correspondence, email: s.ravi.shankar@fz-juelich.de

Abstract

The small-perturbation analysis of perovskite solar cells (PSCs) highlights a fundamental conundrum - while time domain measurements yield two time constants corresponding to the rise and subsequent decay of the photovoltage or photocurrent, the corresponding frequency domain methods only yield one time constant from the analysis of the imaginary part of the transfer function. To solve this problem, we propose a modification of the frequency domain transfer function that focusses on the transition of its real part to negative values at high frequencies. After verification using drift-diffusion simulations and equivalent circuit analysis, the application of the method to experimental intensity-modulated photovoltage spectroscopy data of a PSC allows calculation of the hidden rise time constant, showing a good agreement with rise time constants obtained from transient photovoltage measurements. The calculated rise time constants are indicators of the charge extraction efficiency of the contacts, that determines short circuit and low-bias recombination losses.

1. Introduction

Small perturbation techniques are powerful tools for the analysis of physical mechanisms in perovskite solar cells (PSCs). The main advantage of using a small perturbation is the possibility to linearise the mathematical description of higher-order processes, thereby facilitating the data analysis. In the time domain, these techniques include transient photovoltage (TPV) and transient photocurrent (TPC) measurements, that record the rise and subsequent decay of the external voltage and current respectively, as a function of time after the application of a short laser pulse. The corresponding frequency domain techniques are intensity-modulated photovoltage spectroscopy (IMVS), intensity-modulated photocurrent spectroscopy (IMPS) and impedance spectroscopy (IS).

Among the time domain techniques, TPV is widely used to study PSCs, where the decay of the photovoltage is typically fitted with a mono or bi-exponential function, with the corresponding characteristic time constants subsequently assigned to different physical mechanisms such as trap-mediated recombination and recombination limited by the injection of electrode charges.[1, 2, 3, 4] The rise time of the photovoltage is typically not analysed in the PSC community, though its time constant has been interpreted as the charge carrier transport time from the bulk to the electrodes in the case of dye-sensitized solar cells.[5] Recently, Krückemeier et al. have shown that the photovoltage rise time in PSCs is determined by the speed of charge carrier exchange between the perovskite absorber and the electrodes via the transport layers.[6] In the case of frequency domain methods, the typical approaches for data analysis are based on using models such as the diffusion-recombination model,[7, 8, 9] fitting of equivalent circuits[10, 11, 12, 13] and calculation of time constants as a function of DC parameters.[14, 15, 16, 17] In the case of IS, the analysis of the capacitance and its evolution versus angular frequency ω and DC voltage are also used to obtain parameters such as doping and defect densities.[18] Irrespective of the different analysis methods, the same information is expected to be contained in a time domain measurement and its corresponding frequency domain measurement (e.g. TPV → IMVS), since

1

the time domain data can be converted to the frequency domain using a Laplace transform, which is a lossless transformation.[19] However, this equivalence between the time and frequency domain methods has not been established experimentally.

In this work, we connect the analysis methods for both the time domain and frequency domain small perturbation techniques through the analysis of their characteristic time constants. We find that while the time-domain methods (TPV and TPC) naturally yield two time constants that correspond to the rise and subsequent decay of the photovoltage or photocurrent, the corresponding frequency domain methods of IMVS and IMPS yield only one time constant, the decay time constant, from the traditional analysis method. To identify the hidden rise time constant in the frequency domain data, we propose a modification of the transfer functions by a factor of $i\omega$. Using drift-diffusion simulations and equivalent circuit analysis, we show that the transformation allows clearly observing both the rise and decay time constants, from the frequency extrema of the imaginary part of the modified transfer function. We further apply this method to experimental IMVS spectra of a perovskite solar cell, identifying similar magnitudes of the two time constants compared to the corresponding TPV measurements. We thus prove that the same information is contained in both the time and frequency domain spectra, albeit in different forms. Furthermore, the rise time constant unveiled from the frequency domain data is related to the efficacy of charge extraction by the transport layers, allowing for accurate characterization of short-circuit and low forward bias losses that strongly affect the fill factor of the PSC's current-voltage curve.

Definitions

In a TPV measurement, the device is held at open circuit (typically using a load resistance of 1MΩ) under a given DC illumination, and a short pulse of photons is impinged on it. The deflection ΔV_{ext} of the external voltage V_{ext} is subsequently recorded as a function of time t. As there is no current flowing across the terminals at open circuit, V_{ext} is equal to the difference between the electron quasi-Fermi level at the cathode minus the hole quasi-Fermi level at the anode (referred to as V_{elec}). For the case of TPC measurements, the load resistance is reduced to typically 50 Ω and the current deflection Δj_{ext} (where j_{ext} is the current density at the terminals) is measured using an oscilloscope. The frequency-domain counterparts of TPV and TPC are IMVS and IMPS respectively – IMVS measures the AC external voltage while IMPS measures the AC current at the terminals upon application of an AC small perturbation of photon flux Φ (represented as a current density $j_\Phi = q\Phi$). The IMVS transfer function is thus given by

$$W = \frac{\tilde{V}_{\text{ext}}}{\tilde{j}_\Phi} \tag{1}$$

and the IMPS transfer function is given by

$$Q = \frac{\tilde{j}_{\text{elec}}}{\tilde{j}_\Phi}, \tag{2}$$

where the tilde represents an AC quantity. A third transfer function called the impedance is defined by measuring the AC terminal current upon the application of an AC small perturbation of the external voltage, given by

$$Z = \frac{\tilde{V}_{\text{ext}}}{\tilde{j}_{\text{elec}}}. \tag{3}$$

In general, these methods can be measured at any DC condition, however, IMPS is traditionally measured at short circuit[20] while IMVS is measured at open circuit[21] (IS is measured across a range of DC conditions)[22]. The frequency domain data are usually represented by plotting the real versus the negative imaginary part of the transfer function (hereafter termed $W/Q/Z$ - plane plot depending on the transfer function). Figures 1(a,b) show simulated TPV and TPC data respectively of a typical p-i-n PSC and figures 1(c-e) show the corresponding simulated IMVS,

IMPS and IS spectra respectively (see table S1 and section A1 in the supporting information (SI) for simulation parameters and their discussion). For simplicity, we do not include mobile ions in the simulations in figure 1.
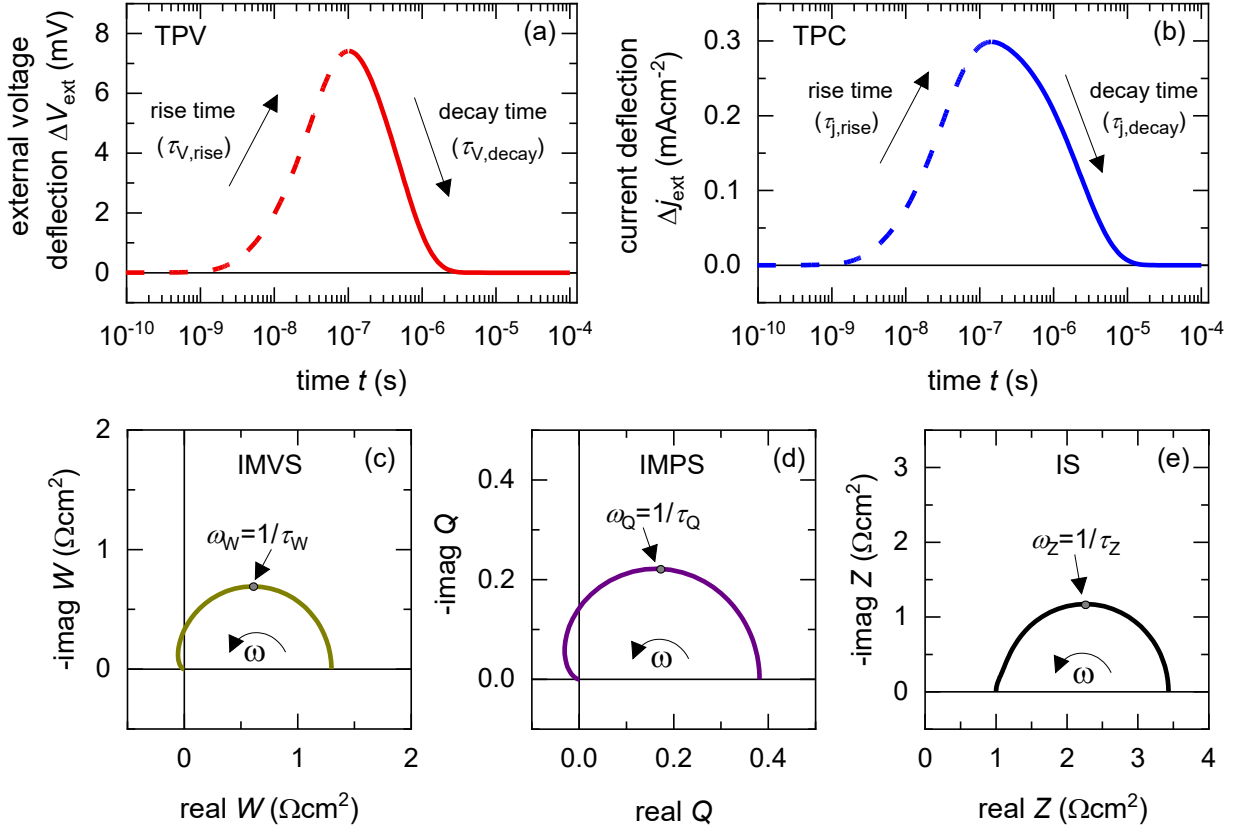
Figure 1 Typical representation of the data obtained from the time and frequency domain measurements. Drift-diffusion simulations of (a) transient photovoltage (TPV) and (b) transient photocurrent (TPC) spectra of a p-i-n perovskite solar cell that shows the voltage deflection and current deflection respectively upon application of a laser pulse at $t = 0$. Dashed lines show the rise of the photovoltage/photocurrent that is governed by the rise time constant while solid lines show the decay of the photovoltage/photocurrent governed by the decay time constant. Simulated (c) intensity-modulated photovoltage spectroscopy (IMVS), (d) intensity-modulated photocurrent spectroscopy (IMPS) and (e) impedance spectroscopy (IS) spectra of the same solar cell. The corresponding characteristic time constants obtained from the maxima of the negative imaginary part of the transfer function is also shown. See table S1 in the SI for simulation parameters.

2. Results

A. Connection between time and frequency domain spectra

In this section, we will analyse the data in figure 1 with the goal of accurately modelling the device physics and hence obtaining parameters of photovoltaic operation. We first analyse drift-diffusion simulations of the TPV and TPC spectra in figures 1(a,b), for a p-i-n perovskite solar cell. In both cases, we see a rise of the photovoltage or the photocurrent upon application of the laser pulse, which then reaches a peak followed by a decay back to the steady-state value. In the PSC community, only the decay of the photovoltage or photocurrent is typically analysed by fitting an exponential to obtain the characteristic decay time constant.[1, 2, 4, 23] However, in the case of dye-sensitized solar cells, the characteristic rise time constants of the photovoltage were analysed and attributed to electron transport across the TiO₂ layer[5] while for organic solar cells,

3

the rise of the photocurrent was analysed to get insight into charge trapping.[24, 25] In the simplest scenario, we can assume that both the rise and decay occur exponentially, where the rise of the quantity is proportional to $1 - \exp\left(-t/\tau_{\text{rise}}\right)$, while the decay is proportional to $\exp\left(-t/\tau_{\text{decay}}\right)$. We can thus describe the external voltage deflection ΔV_{ext} as

$$\Delta V_{\text{ext}}(t) = \Delta V_{\text{ext},0} \left(e^{\frac{-t}{\tau_{\text{V,decay}}}} - e^{\frac{-t}{\tau_{\text{V,rise}}}} \right), \tag{4}$$

and the photocurrent deflection Δj_{ext} as

$$\Delta j_{\text{ext}}(t) = \Delta j_{\text{ext},0} \left(e^{\frac{-t}{\tau_{\text{j,decay}}}} - e^{\frac{-t}{\tau_{\text{j,rise}}}} \right). \tag{5}$$

In equations 4 and 5, τ_{rise} and τ_{decay} are characteristic time constants that determine the speed of the rise or decay of the measured quantity respectively, hereafter referred to as rise and decay time constants. $\Delta V_{\text{ext},0}$ and $\Delta j_{\text{ext},0}$ are the peak photovoltage and photocurrent deflections respectively, that are also a function of the laser pulse intensity. The validity of equations 4 and 5 have been proven in refs.[6, 26], for situations where the laser pulse width in time is much faster than the photovoltage or photocurrent rise time. These refs. developed a model that accounts for charge carrier exchange between the perovskite absorber and the electrodes through the transport layers, in addition to typical recombination and capacitive effects. This charge carrier exchange is crucial to build up the external voltage in a TPV measurement or drive the photocurrent in a TPC measurement.

In the case of the frequency domain spectra in figures 1(c-e), the characteristic frequencies ω_{char} are obtained from the frequency of the maxima of the negative imaginary part versus angular frequency ω ($\omega = 2\pi f$, where f is the frequency in Hz), allowing to calculate the characteristic time constants τ_{char} using

$$\frac{d(-\text{im transfer function})}{d\omega} = 0 \rightarrow \omega_{\text{char}} = \frac{1}{\tau_{\text{char}}}. \tag{6}$$

Alternately, the frequency of the maxima of the negative imaginary part can also be obtained from the maxima of the y-axis in the $W/Q/Z$-plane plot, which corresponds to the top of the arc or arcs observed in these plots, as shown in figures 1(c-e). We note that there are other methods of data analysis, such as the direct fitting of the diffusion-recombination model[7, 8] or the analysis of capacitance steps versus time[27] or frequency[28] and equivalent circuit fitting.[11, 12] However, these methods are limited by the fact that a model or equivalent circuit needs to be assumed, which is unclear in the case of PSCs. Therefore, we promote the method of studying the evolution of the measured time constants as a function of DC parameters such as external voltage, current density and light intensity, which can then be associated to fundamental physical mechanisms based on their characteristic evolution versus DC parameters. Such an analysis method ensures no loss of information arising from assuming models or equivalent circuits.

We begin our analysis by comparing the time constants obtained from drift-diffusion simulations of the TPV and IMVS spectra of a p-i-n perovskite solar cell at DC open-circuit condition under 100 mW/cm^2 illumination using a blue LED (459 nm), for different mobilities of the transport layers. For simplicity, the simulations assume the ETL and HTL mobility to be equal and do not consider any mobile ionic densities within the perovskite layer. The permittivity of the perovskite layer was arbitrarily increased to emulate a situation where the ions completely screen the electric field. The influence of Shockley-Read-Hall (SRH) recombination[29] is simulated using a density of mid-gap traps (parameters shown in table S1 in the SI). Figure 2(a) shows that the rise of the photovoltage is strongly dependent on the mobility of the transport layers, with faster rises and higher peaks in the photovoltage observed for increasing mobilities of the transport layers. This is because charge carriers are transported from

4

the perovskite layer to the electrodes via the electric field in the transport layers (see figure S1 in the SI for band diagram) to build up the photovoltage or drive the photocurrent. The decay of the photovoltage is mostly independent of the transport layer mobility, indicating that the dominant mechanism is bulk recombination. We note that the calculation of recombination lifetimes from the decay time constants is limited by charge carrier redistribution in the case of low mobility of charge carriers in the absorber layer, as in the case of organic solar cells.[30] However, this limitation does not apply for thin-film PSCs due to the large mobilities or diffusion coefficients of the charge carriers.[31, 32]

The corresponding IMVS spectra in figure 2(b) show a single arc in the W-plane plot for all cases. For lower transport layer mobilities, the real part of W shows a pronounced transition (larger amplitudes) to the second quadrant, showing a negative value at high frequencies before reaching the origin. The occurrence of a single arc in the W-plane plot implies one observable time constant from IMVS, whereas the rise and decay of the photovoltage implies two time constants from TPV measurements (see figure S2 in the SI for fitting using equation 4). Figure 2(c) shows that there is a good agreement between the slower time constant (decay time constant) from TPV and IMVS, which approaches the SRH recombination lifetime (τ_{SRH}) for higher transport layer mobilities. The faster time constant, which corresponds to the rise time constant, shows a strong dependence on the transport layer mobility, rising from a few nanoseconds when the transport layer mobilities equal that of the perovskite to 100 nanoseconds for the lowest transport layer mobility chosen.
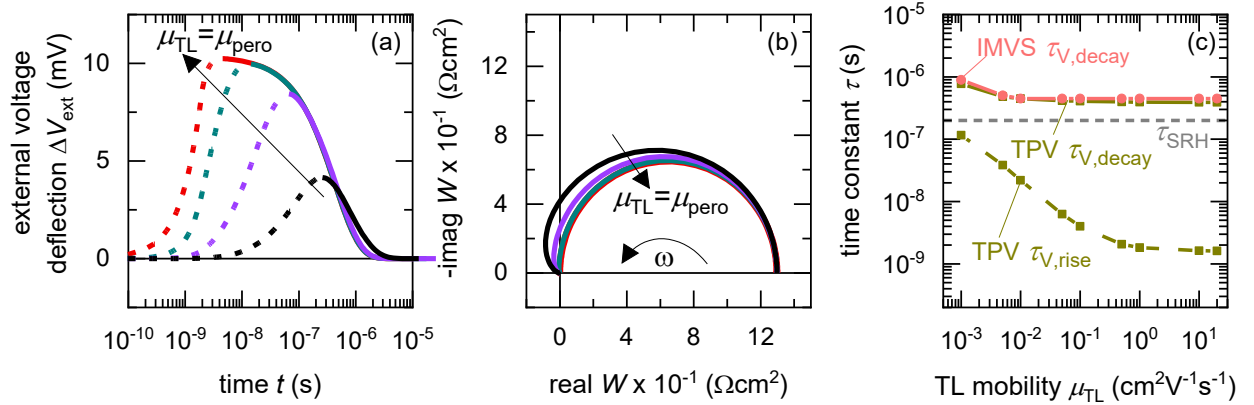
Figure 2 Calculation of time constants from the time and frequency domain data. Drift-diffusion simulations of (a) TPV and (b) IMVS spectra at DC open-circuit conditions under 100 mW/cm^2 illumination with a blue LED (459 nm), for different transport layer mobilities. (c) shows the corresponding calculated rise (dashed lines) and decay (solid lines) time constants from fitting the TPV spectra using equation 4 (fitting shown in figure S2 in the SI), and the IMVS time constant (circles) obtained from (b) using equation 6. While TPV yields both the rise and decay time constants, IMVS yields only the decay time constant. The transport layer mobilities were set equal for simplicity and no ionic densities were considered in the perovskite layer. The permittivity of the perovskite layer was arbitrarily increased to simulate the situation where the ions screen the electric field. Simulation parameters are shown in table S1 in the SI. For clarity, only a few of the simulated spectra are shown in (a) and (b).

However, figure 2 raises the question – *why is the rise time constant observed in the time domain but not in the frequency domain*? Since the transformation from the time domain to the frequency domain is a lossless one, we conclude that the rise time constant is hidden in the frequency domain data. This effect can be understood by taking the Laplace transform of equation 4, which yields the IMVS transfer function

$$W = W_0 \left(\frac{\tau_{V,decay}}{1+i\omega\tau_{V,decay}} - \frac{\tau_{V,rise}}{1+i\omega\tau_{V,rise}} \right), \tag{7}$$

where W_0 is a constant with the unit Ωcm^2. For time constants well-separated in magnitude ($\tau_{V,decay} \gg \tau_{V,rise}$), the first term in the RHS of equation 7 is much bigger than the second term. In such a situation, the second term in the RHS drops out (see section A2 in the SI for derivation) and the characteristic time constant calculated from the frequency maximum of the negative imaginary part of W is

$$\tau_{char}(\tau_{V,decay} \gg \tau_{V,rise}) = \frac{1}{\omega_{char}} = \tau_{V,decay}, \tag{8}$$

Equation 8 shows that the rise time constant cannot be observed from the typical analysis of the frequency maximum of the negative imaginary part of the transfer function when it is significantly smaller than the decay time constant. Since the rise time constant is in many cases related to charge extraction from the absorber to the contacts, the situation where $\tau_{V,decay} \gg \tau_{V,rise}$ is likely to be frequently encountered, especially at low forward biases.[26, 6] Therefore, even though the transfer function contains two time constants, only the slower time constant is expressed, leading to a single arc in the frequency domain spectrum. We thus require a data analysis method that allows visualising both time constants clearly. In the case of time domain measurements, we note that both the absolute value and the slope of the photovoltage or photocurrent can be obtained from the plot of photovoltage or photocurrent versus time. In the case of frequency domain measurements, the slope of the real part of the transfer function is not defined and hence not analysed. Based on this intuition, we define a new transfer function

$$M_W = i\omega W = -\omega(\text{imag } W) + i\omega(\text{real } W), \tag{9}$$

whose imaginary part is the product of the angular frequency and the real part of the IMVS transfer function W. Using equation 7 in equation 9, we obtain

$$-\text{imag } M_W = W_0 \left(\frac{\omega\tau_{V,rise}}{1+\omega^2\tau_{V,rise}^2} - \frac{\omega\tau_{V,decay}}{1+\omega^2\tau_{V,decay}^2} \right). \tag{10}$$

Figures 3(a,b) show the simulated negative imaginary parts of W and M_W versus angular frequency for different transport layer mobilities of the PSC. While $-\text{imag } W$ shows only one peak that corresponds to a single time constant, $-\text{imag } M_W$ shows a peak each in the upper and lower quadrant that corresponds to two time constants (see section A3 in the SI for derivation). The additional time constant is obtained from the region at high frequencies where the real part of the IMVS transfer function W transitions to a negative value (i.e. moves to the second or third quadrant), consequently making a peak in the opposite quadrant to that of the decay time in figure 3(b). Therefore, while the transition to the negative real part of the transfer function has been attributed to different physical mechanisms such as diffusion,[7] trapping[33] and ionic effects,[34] this effect arises from a simple consideration of a rise and decay time constant in a transient measurement. The amplitude of this transition to the negative real part is proportional to the rise time constant (see derivation in section A4 in the SI), which is also observed from figures 2(a) and 2(b) for lower transport layer mobilities, which show larger (slower) rise time constants. Figure 3(c) shows that the additional time constant obtained from M_W is indeed the rise time constant calculated from the TPV data (figure 2(a)), while the slow time constant is obtained from both W and M_W. In summary, the transformation of the IMVS transfer function from W to M_W allows determination of both the rise and decay time constants. We note that the divergence in the calculated rise time constants from both TPV and IMVS occurs only when the rise time constants are of the order of the time width of the laser pulse (2 ns) in the TPV simulation.
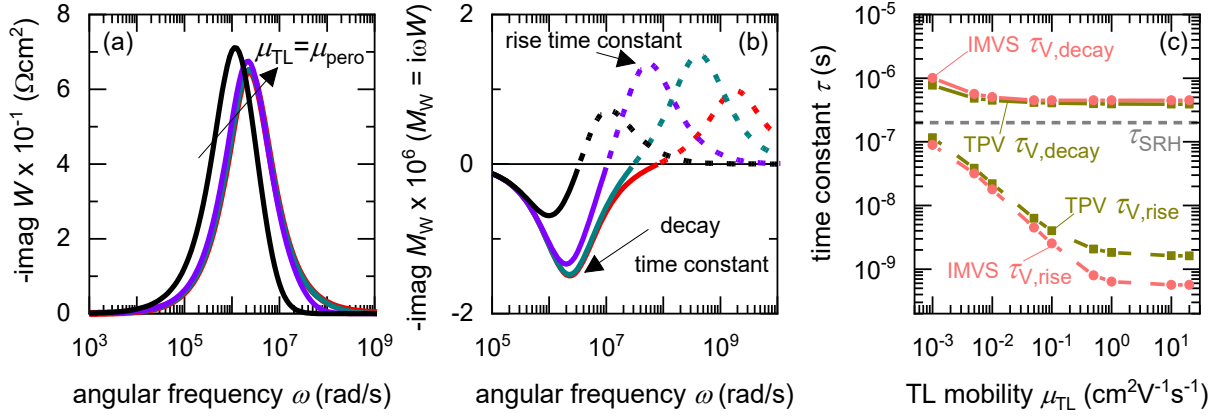
Figure 3 Transformation of IMVS data to obtain the rise and decay time constants. Drift-diffusion simulations of the negative imaginary part of (a) IMVS transfer function W and (b) transformed transfer function $M_W = i\omega W$ versus angular frequency ω, for different transport layer mobilities μ_{TL}. The negative imaginary part of M_W shows both the rise (dashed lines) and decay (solid lines) time constants, while that of W only shows the decay time constant. (c) shows the calculated rise and decay time constants from the negative imaginary part of M_W in (b) and the TPV simulations in figure 2. The calculated rise and decay time constants from both the TPV and the transformed IMVS data are almost identical. For clarity, only a few of the simulated spectra are shown in (a) and (b).

We now increase the complexity of the TPV and IMVS simulations by reducing the permittivity of the perovskite to $\varepsilon_r = 30$ to allow the existence of an electric field and by including equal densities of mobile cations and anions. The TPV, IMVS simulations and the calculated time constants are shown in figure S3 in the SI. The IMVS spectra now show an additional arc at low frequencies due to the mobile ions, which leads to an additional time constant in this frequency range.[35] The calculated rise and decay time constants remain unaffected even after inclusion of the mobile ionic densities, at this DC open-circuit condition. The calculated rise and decay time constants from IMVS match nicely with those from TPV, confirming the validity of our model in situations with mobile ionic densities in the perovskite layer.

B. Time constants from IMVS, IMPS and IS

In this section, we will verify the validity of the developed analysis method by using it to extract the time constants from the typical frequency domain spectra (IMVS, IMPS and IS), using an equivalent circuit of the PSC, shown in figure 4. This equivalent circuit is derived from a kinetic model of the PSC developed in ref.[26], that focusses on the electronic response occurring at higher frequencies and ignores the low-frequency response related to mobile ions in the perovskite layer. The model considers a high mobility,[31] thin-film, intrinsic perovskite absorber of thickness d_{pero} sandwiched between symmetric, low-mobility (in comparison to the perovskite layer) electron and hole transport layers. The model further assumes that the bulk of the perovskite layer is electric field-free due to the shielding by the mobile ionic density.[36] The transport layers are modelled using a charge exchange velocity S_{exc} that determines the speed of charge carrier transfer between the perovskite and the electrodes, through the transport layers. This leads to a charge carrier exchange resistance R_{exc} that determines the potential drop across the transport layers, given by[26]

$$R_{exc} = \frac{2k_B T}{q^2 n_{int} S_{exc}(V_{elec})} \exp\left(-\frac{qV_{elec}}{2k_B T}\right), \tag{11}$$

where V_{elec} is the quasi-Fermi level splitting of the electrons at the cathode minus the quasi-Fermi level splitting of the holes at the anode and n_{int} is the charge carrier concentration at the

perovskite/transport layer interface. The charge carrier exchange velocity S_{exc} is given by[37]

$$S_{exc}(V_{elec}) = \frac{\mu_{TL}F_{TL}}{1-\exp\left(-\frac{qF_{TL}d_{TL}}{k_BT}\right)}, \tag{12}$$

where μ_{TL} and F_{TL} are the mobility and electric field in the transport layer respectively, and d_{TL} is the thickness of the transport layer. For situations of large electric field in the transport layer, $S_{exc} \cong \mu_{TL}F_{TL}$ is the drift velocity. We also define a charge carrier exchange lifetime τ_{exc} that is given by

$$\tau_{exc} = \frac{d_{pero}}{S_{exc}} = R_{exc}C_\mu, \tag{13}$$

where C_μ is the chemical capacitance[38], given by

$$C_\mu = \left(\frac{q^2 dn}{2k_BT}\right) = C_{\mu,0}\exp\left(\frac{qV_{int}}{2k_BT}\right). \tag{14}$$

Bulk recombination is modelled using the effective recombination lifetime τ_{eff}, that consists of the parallel combination of the radiative and SRH lifetime

$$\tau_{eff} = \left(\frac{1}{\tau_{rad}} + \frac{1}{\tau_{SRH}}\right)^{-1} = \left(\frac{1}{\left(\frac{1}{2B_{rad}n}\right)} + \frac{1}{\tau_{SRH}}\right)^{-1}, \tag{15}$$

where B_{rad} is the radiative recombination coefficient (cm^3/s), n is the carrier concentration and $V_{int} = (E_{Fn} - E_{Fp})/q$ is the steady-state average quasi-Fermi level splitting in the perovskite layer, referred to as the internal voltage. The factor 2 in the denominator of equations 14 and 15 is due to the intrinsic nature of the perovskite. The recombination resistance is thus given by

$$R_{rec} = \frac{\tau_{eff}}{C_\mu}. \tag{16}$$

The model is completed by the inclusion of an external series resistance R_s and the geometric capacitance C_g. The equivalent circuit derived from the model is shown in figure 4. The IMVS, IMPS and IS transfer functions are calculated (photogeneration across the $R_{rec}||C_\mu$ line) from the equivalent circuit as

$$W = \left(\frac{1}{R_{rec}} + i\omega C_\mu + i\omega C_g\left(1 + \frac{R_{exc}}{R_{rec}} + i\omega R_{exc}C_\mu\right)\right)^{-1}, \tag{17}$$

$$Q = \left(1 + \frac{R_s+R_{exc}}{R_{rec}} + i\omega(R_s + R_{exc})C_\mu + i\omega R_sC_g\left(1 + \frac{R_{exc}}{R_{rec}} + i\omega R_{exc}C_\mu\right)\right)^{-1}, \tag{18}$$

$$Z = R_s + \left(\frac{1}{R_{exc}+\left(\frac{1}{R_{rec}}+i\omega C_\mu\right)^{-1}} + i\omega C_g\right)^{-1} = \frac{W}{Q}. \tag{19}$$

8
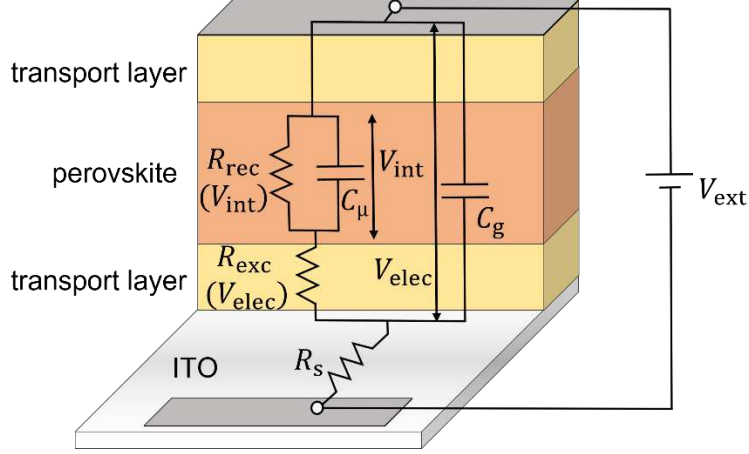
Figure 4 Equivalent circuit of the perovskite solar cell. Derived equivalent circuit from the model in section 2(B), used to verify the validity of the transformation method described in section 2(A). R_{rec} is the recombination resistance (equation 16), R_{exc} is the charge carrier exchange resistance (equation 11) that models the potential drop across the transport layers, R_s is the series resistance, C_μ is the chemical capacitance (equation 14) and C_g is the geometric capacitance of the perovskite layer. The model used to derive the equivalent circuit is described in section 2(B) and extensively in ref.[26].

We thus generalise the transformation method described in section 2(A) and extend it to the IMPS and IS transfer functions. In case of IS, the series resistance is subtracted from the total impedance and then transformed to M_Z to obtain the time constants. This is because while the characteristic frequency of the impedance transfer function Z is independent of R_s, the characteristic frequency of the modified transfer function M_Z is dependent on R_s in the form of a linear, additive term and hence needs to be subtracted out to remove its influence (see section A5 in the SI for derivation). A summary of these transfer functions and their transformations to obtain the rise and decay time constants are shown in table 1.

Table 1 Summary of frequency domain transfer functions and their corresponding transformations to obtain the rise and decay time constants from the data.

Transfer function	Transformation	Time constants
W(IMVS)	$M_W = i\omega W$	extrema of $-$imag M_W versus ω
Q (IMPS)	$M_Q = i\omega Q$	extrema of $-$imag M_Q versus ω
Z (IS)	$M_Z = i\omega(Z - R_s)$	extrema of $-$imag M_Z versus ω

   Figures 5(a-c) show the calculated rise and decay time constants from simulations of the IMVS, IMPS and IS spectra respectively using the equivalent circuit in figure 4 (see table S2 in the SI for parameters and figure S4 in the SI for the peaks in the negative imaginary part of the modified transfer functions that correspond to the two time constants). The IMVS and IS response are identical, with the rise time constant corresponding to τ_{exc} at low open-circuit voltages followed by a transition to the product $R_{exc}C_g$, causing it to exponentially decrease at large open-circuit voltages. The decay time constant follows the effective recombination lifetime τ_{eff}, decreasing exponentially at large open-circuit voltages followed by a very short saturation at lower open-circuit voltages. This corresponds to the dominance of radiative recombination at high open-circuit voltages and SRH recombination at lower open-circuit voltages. The short saturation in the decay time constant is rapidly followed by an exponential

9

increase at lower open-circuit voltages corresponding to the product $R_{rec}C_g$. This effect has been observed and analysed from both electrical and luminescence methods,[3, 4, 39, 40] where the recombination is limited by the back-injection of charges from the electrodes into the absorber. In the case of IMPS, the rise time constant is identical to that of IMVS and IS, while the decay time constant corresponds to τ_{eff} at large open-circuit voltages and transitions to the product R_sC_g (generally called RC attenuation) at low open-circuit voltages. Thus, our new method for data analysis of frequency domain spectra allows determination of the rise time constant, which was inaccessible from the standard analysis of the imaginary part of the transfer function. The rise time constant contains information regarding the extraction of charges from the perovskite layer to the electrodes and is a function of transport layer parameters such as the mobility and built-in voltage (equations 12 and 13).
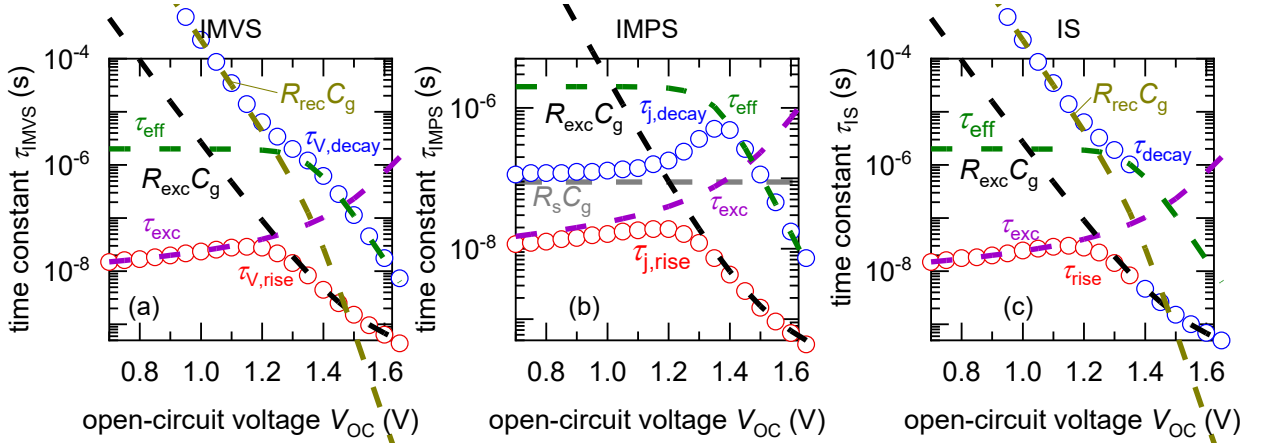

Figure 5 Simulated time constants from an equivalent circuit. Calculated rise time constants $\boldsymbol{\tau_{rise}}$ (red, open circles) and decay time constants $\boldsymbol{\tau_{decay}}$ (blue, open circles) versus DC open-circuit voltage, obtained from simulated (a) IMVS, (b) IMPS and (c) IS spectra of the equivalent circuit in figure 4, using the transformation method discussed in section 2(A) and summarised in table 1. These time constants correspond to different $\boldsymbol{RC}$ products as shown, depending on the DC open-circuit voltage. $\boldsymbol{R_s}$ is the series resistance, $\boldsymbol{R_{rec}}$ is the recombination resistance (equation 16), $\boldsymbol{R_{exc}}$ is the exchange resistance that models the potential drop across the transport layers (equation 11), $\boldsymbol{C_g}$ is the geometric capacitance, $\boldsymbol{\tau_{eff}}$ is the effective recombination lifetime (equation 15) and $\boldsymbol{\tau_{exc}}$ is the charge carrier exchange lifetime (equation 13). The parameters used for the equivalent circuit simulations are summarised in table S2 in the SI.

C. Analysis of experimental spectra

We now proceed to study experimental TPV and IMVS spectra obtained from measurements of p-i-n thin film perovskite solar cells, using our developed analysis method. The structure of the samples used were ITO/SAMs/PTAA/Cs$_{0.05}$FA$_{0.8}$MA$_{0.15}$PbI$_{2.25}$Br$_{0.75}$/C$_{60}$/BCP/Ag (fabrication details provided in the methods section, current-voltage curves provided in figure S5 in the SI), where SAMs is a mixture of self-assembled monolayers (Me-4PACz and MeO-2PACz), poly(triaryl amine) (PTAA) is the hole transport layer and C$_{60}$/BCP (Bathocuproine) is the electron transport layer. For both the TPV and IMVS measurements, the spectra were collected at different DC bias light intensities under open-circuit conditions, with the open-circuit condition set using a 1 MΩ load resistor (further experimental details provided in the methods section).

Figure 6(a) shows an example of the W-plane plots of the IMVS transfer function, measured at different open-circuit voltages (see figure S6 in the SI for all IMVS and TPV spectra). These plots show the same general shape, consisting of two arcs, one at high frequency and one at low frequencies below $\cong$ 500 Hz. The low-frequency arc in frequency domain spectra has been

well-studied and is attributed to ionic effects in the PSC.[35] The high frequency arc shows the same behaviour as seen from the simulations in figure 2(b), with a transition to a negative real part of the transfer function at high frequencies. Based on the analysis in section 2(A), we conclude that the high frequency arc arises from electronic effects and contains the rise and decay time constants of the photovoltage. We thus transform the IMVS transfer function to M_W and analyse the evolution of the negative imaginary part of M_W versus angular frequency ω, shown in figure 6(b). We observe peaks in the positive and negative directions, which correspond to the rise and decay time constants of the photovoltage. Figure 6(c) shows an example of the measured TPV spectra at different open-circuit voltages and their corresponding fitting with equation 4 to obtain the rise and decay time constants of the photovoltage in the time domain. We note that the rise of the photovoltage at short times is affected by ringing effects due to reflections of the output voltage at the 1 MΩ load resistance.
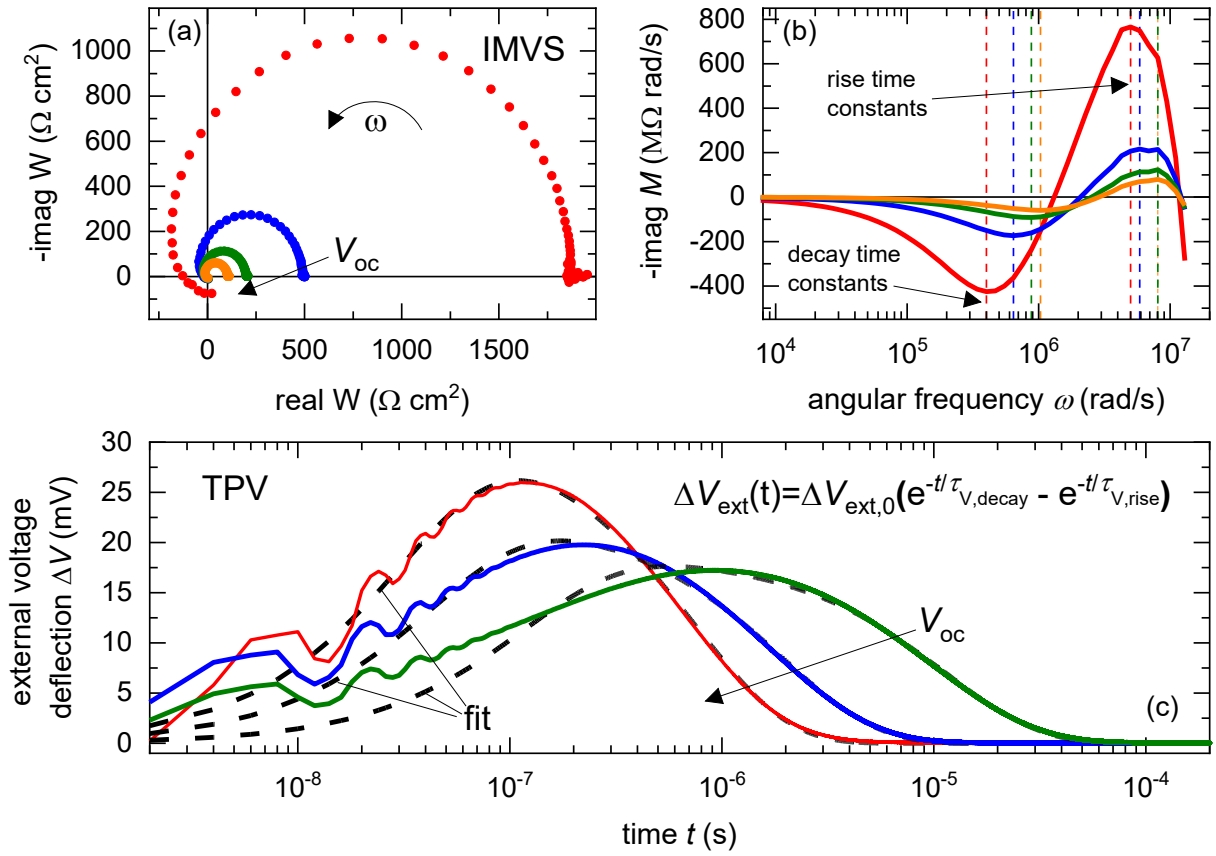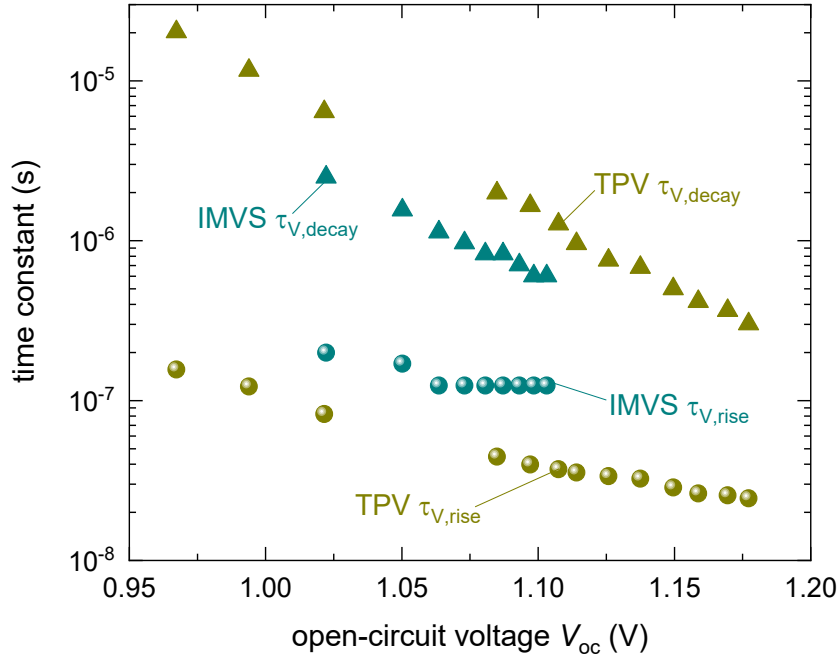

Figure 6 Analysis of experimental IMVS and TPV spectra of perovskite solar cells. Measured (a) real versus negative imaginary part of the IMVS transfer function $\mathbf{W}$ and (b) negative imaginary part of transformed IMVS transfer function ($\mathbf{M_W = i\omega W}$) versus angular frequency $\boldsymbol{\omega}$ and (c) TPV spectra of $Cs_{0.05}FA_{0.8}MA_{0.15}PbI_{2.25}Br_{0.75}$ perovskite solar cells, measured at different DC open-circuit voltages using the PAIOS instrument developed by Fluxim. The data in (c) was fitted using equation 4 to obtain the rise and decay time constants. The frequencies of the peaks in (b) (dashed lines) correspond to the rise and decay time constants of the photovoltage. The entire set of measured spectra shown in figure S6 in the SI.

Figure 7 shows the calculated rise and decay time constants of the photovoltage from both TPV and IMVS measurements. The time constants from both methods show a good agreement with each other. To identify the physical mechanisms that generate these time constants, we define a slope factor θ using

11

$$\tau = \tau_0 \times exp\left(\frac{-qV_{oc}}{\theta k_B T}\right), \qquad (20)$$

where τ_0 is a constant with a unit of seconds. Depending on the coupling between the voltage-dependent and voltage-independent resistances and capacitances described in section 2(B), different values of the slope factor are expressed, allowing to differentiate the mechanisms. Figure S7 in the SI shows the calculated slope factors for the measured time constants of IMVS and TPV. The decay time constant $\tau_{V,decay}$ from both IMVS and TPV shows an exponential evolution versus open-circuit voltage with a slope factor close to 2. This corresponds to a time constant that is limited by the first-order recombination of charge carriers that are re-injected into the intrinsic perovskite layer from the electrodes, expressed as the product of the recombination resistance R_{rec} (equation 16) and the geometric capacitance C_g.[3, 4, 26, 40] The rise time constant $\tau_{V,rise}$ from TPV remains approximately constant at high open-circuit voltages (large slope factor θ =5.97), with a magnitude of $\tau_{V,rise} \cong 4 \times 10^{-8}$ s. At lower open-circuit voltages, a small increase in magnitude is observed. A similar evolution and magnitude of the rise time constant was observed from TPV measurements on a thin-film $CH_3NH_3PbI_3$ solar cell.[6] For the corresponding voltage range, $\tau_{V,rise}$ from IMVS shows a similar behaviour with a larger magnitude of $\tau_{V,rise} \cong 10^{-7}$ s. Based on the model discussed in section 2(B) and the large slope factor, we conclude that the rise time constant corresponds to the exchange lifetime τ_{exc} (which is also not independent of V_{elec}, see equation 13). τ_{exc} determines the speed at which charge carriers are transferred from (to) the perovskite to (from) the electrodes through the transport layers. The voltage dependence and absolute value of the ratio of τ_{exc} to the recombination lifetime τ_{eff} (equation 15) has been shown to significantly affect the fill factor, since it determines the magnitude and voltage-dependence of recombination losses at short-circuit and low forward bias.[6, 41]

Figure 7 Calculated rise and decay time constants from the experimental IMVS and TPV spectra. The triangles correspond to the decay time constants while the spheres correspond to the rise time constants. Based on their slope factors $\boldsymbol{\theta}$ calculated using equation 20 (see figure S7 in the SI for fitting), the decay time constant is ascribed to recombination of charge carriers back-injected by the electrodes, while the rise time constant is ascribed to the speed of charge carrier extraction from the perovskite to the electrodes, via the transport layers.

3. Discussion

Time domain small-perturbation techniques such as transient photovoltage (TPV) and transient photocurrent (TPC), and their frequency domain counterparts – intensity-modulated photovoltage spectroscopy (IMVS), intensity-modulated photocurrent spectroscopy (IMPS) and impedance spectroscopy (IS) are widely used for the characterization of perovskite solar cells (PSCs). However, the different analysis and representation methods for each technique make it difficult to reliably extract information and compare calculated parameters. This effect manifests itself in the case of the measured time constants, where time domain measurements naturally yield two time constants that correspond to the rise and subsequent decay of the photovoltage or photocurrent, while the corresponding frequency domain method yields only one time constant.

We solve this problem by defining a modified transfer function that focusses on the evolution of the real part of the transfer function versus frequency. Analysis of the modified transfer function shows an additional time constant at high frequencies that is invisible in the unmodified transfer function. From drift-diffusion simulations and analysis of an equivalent circuit, we find that this additional time constant corresponds to the rise time constant observed in the time domain measurements, while the time constant observed in the unmodified transfer function is the decay time constant. We further verify the validity of the transformation method by applying it to experimental IMVS data of perovskite solar cells, to obtain both the rise and decay time constants of the photovoltage. These time constants are similar in magnitude to those obtained from TPV measurements, showing the first equivalence between parameters obtained from time domain and frequency domain measurements for PSCs. This result confirms that the same information is contained in both time and frequency domain measurements, although in different forms. Our developed method allows extracting all the time constants that govern the device response as a function of DC parameters, allowing analysis of the device physics without the assumption of a model or equivalent circuit.

Methods
Materials

Cesium iodide (CsI), N,N'-dimethylformamide (DMF), dimethyl sulfoxide (DMSO) and ethyl acetate were purchased from Sigma Aldrich. Self-assembled monolayers Me-4PACz and MeO-2PACz, bathocuproine (BCP, 99.0%), lead iodide (PbI$_2$, 99.99%) were purchased from TCI. Lead bromide (PbBr$_2$, 98%) was purchased from Acros Organics. Formamidinium iodide (FAI) and 4-fluoro-phenethylammonium iodide (F-PEAI) were purchased from Greatcell Solar Materials. Methylammonium bromide (MABr) was obtained from Dyesol. C$_{60}$ was obtained from Ossila. Poly[bis-(4-phenyl)-(2,4,6-trimethylphenyl)-amine] (PTAA, $M_n = 17900$, $M_w = 33000$) was purchased from Xi'an Polymer Light Technology Corp (China).

Device fabrication

The patterned indium doped tin oxide (ITO) substrates (20mm*20mm) from KINTEC were sequentially cleaned through Hellmanex III, deionized water, acetone, and 2-propanol for 10 min each followed by oxygen plasma (Diener Zepto, 100 W) for 10 min and then transferred to a N$_2$-filled glovebox. The solution of mixture of Me-4PACz and MeO-2PACz (1:1) (1 mmol/mL in total in ethanol) was deposited on ITO substrate at 3000 r.p.m for 30 s and then annealed at 100 °C for 10 min. Then the PTAA solution (0.5mg/ml in toluene) was dropped on the substrates at 4000 r.p.m for 30s and annealed at 100 °C for 10 min. The perovskite precursor solution (1.7M for 1000nm thick perovskite film) was prepared by dissolving 22.08mg CsI, 28.5mg MABr, 233.8mg FAI, 190.5mg PbBr$_2$ and 559.5 mg PbI$_2$ in 1mL DMF: DMSO (3:1 vol ratio) solvent. F-PEAI was added into the perovskite precursor solution for passivation (0.8 mg/ml). The perovskite precursor solution was dropped on substrates and spin coated at 2000

13

r.p.m for 40 s then 5000 r.p.m for 4 s. 250 μL ethyl acetate was slightly dropped on the center of the substrate when the spin coating speed reaches 5000 r.p.m. The film then was annealed on a hot plate at 100 °C for 20 min. Finally, 20 nm C_{60}, 8 nm BCP and 80 nm Ag was deposited sequentially in a K.J. Lesker Mini Spectros System attached to the glovebox ($<5\times10^{-6}$ Pa) using a metal shadow mask. The cell area is 0.16 cm^2.

Transient photovoltage (TPV) measurements

A quote from ref.[40] is provided to describe the TPV measurements – "For the transient photovoltage measurements, we used a pulsed UV-solid-state laser (Coherent Flare NX, 343 nm, 1 ns pulse length, 0 to 2 kHz repetition rate, set to 100Hz in our case), which pumps a dye laser (UDL 300 from Lasertechnik Berlin) filled with Coumarin emitting at 498 nm. This radiation passes through an optical fibre and impinges at an angle of 30° on the sample surface. The illumination spot has an elliptical shape with a diameter of 3.8 mm. In addition, a solid-state laser with 532 nm (Coherent Sapphire SF) is used to provide the bias illumination. The resulting voltage transients are measured with an oscilloscope (LeCroy Waverunner HRO 66Zi 600MHz analog bandwidth, 12 Bit analog to digital conversion)." The open-circuit condition was set using a 1MΩ load resistance.

Intensity-modulated photovoltage spectroscopy (IMVS) measurements

IMVS measurements were made using a PAIOS system developed by Fluxim AG. These measurements were made at different open-circuit voltages by varying the light intensity of a white LED. The frequency range used for the measurements was 1- 10^7 Hz. The AC light intensity perturbation was set to 10% of the DC light intensity.

Drift-diffusion simulations

Drift-diffusion simulations were carried out using SETFOS developed by Fluxim AG.

Conflicts of interest
There are no conflicts of interest to declare.

Data availability
Simulation scripts are uploaded to the Zenodo database with the identifier 10.5281/zenodo.8004546. Experimental datasets will be provided by the corresponding author on reasonable request.

References

1. Wheeler, S. et al. Transient optoelectronic analysis of the impact of material energetics and recombination kinetics on the open-circuit voltage of hybrid perovskite solar cells. *J. Phys. Chem. C* **121**, 13496-13506 (2017).

2. Sanchez, R. S. et al. Slow dynamic processes in lead halide perovskite solar cells. Characteristic times and hysteresis. *J. Phys. Chem. Lett.* **5**, 2357-2363 (2014).

3. Kiermasch, D., Baumann, A., Fischer, M., Dyakonov, V. & Tvingstedt, K. Revisiting lifetimes from transient electrical characterization of thin film solar cells; a capacitive concern evaluated for silicon, organic and perovskite devices. *Energy Environ. Sci.* **11**,

14

629-640 (2018).

4. Wang, Z. S., Ebadi, F., Carlsen, B., Choy, W. C. & Tress, W. Transient photovoltage measurements on perovskite solar cells with varied defect concentrations and inhomogeneous recombination rates. *Small Methods* **4**, 2000290 (2020).

5. O'Regan, B. C., Bakker, K., Kroeze, J., Smit, H., Sommeling, P. & Durrant J. R. Measuring charge transport from transient photovoltage rise times. A new tool to investigate electron transport in nanoparticle films. *J. Phys. Chem. B* **110**, 17155-17160 (2006).

6. Krückemeier, L., Liu, Z., Kirchartz, T. & Rau, U. Quantifying charge extraction and recombination using the rise and decay of the transient photovoltage of perovskite solar cells. *Adv. Mater.* **n/a**, 2300872 (2023).

7. Bou, A. et al. Extracting in Situ charge carrier diffusion parameters in perovskite solar cells with light modulated techniques. *ACS Energy Lett.* **6**, 2248-2255 (2021).

8. Laird, J. S., Ravishankar, S., Rietwyk, K. J., Mao, W., Bach, U. & Smith, T. A. Intensity modulated photocurrent microspectroscopy for next generation photovoltaics. *Small Methods* **6**, 2200493 (2022).

9. Peng, W., Aranda, C., Bakr, O. M., Garcia-Belmonte, G., Bisquert, J. & Guerrero, A. Quantification of ionic diffusion in lead halide perovskite single crystals. *ACS Energy Lett.* **3**, 1477-1481 (2018).

10. Riquelme, A. J., Valadez-Villalobos, K., Boix, P. P., Oskam, G., Mora-Seró, I. & Anta, J. A. Understanding equivalent circuits in perovskite solar cells. Insights from drift-diffusion simulation. *Phys. Chem. Chem. Phys.* **24**, 15657-15671 (2022).

11. Ravishankar, S., Aranda, C., Sanchez, S., Bisquert, J., Saliba, M. & Garcia-Belmonte, G. Perovskite solar cell modeling using light-and voltage-modulated techniques. *J. Phys. Chem. C* **123**, 6444-6449 (2019).

12. Alvarez, A. O., Ravishankar, S. & Fabregat-Santiago, F. Combining modulated techniques for the analysis of photosensitive devices. *Small Methods* **5**, 2100661 (2021).

13. Guerrero, A., Bisquert, J. & Garcia-Belmonte, G. Impedance spectroscopy of metal halide perovskite solar cells from the perspective of equivalent circuits. *Chem. Rev.* **121**, 14430-14484 (2021).

14. Todinova, A., Idígoras, J., Salado, M., Kazim, S. & Anta J. A. Universal features of electron dynamics in solar cells with TiO_2 contact: from dye solar cells to perovskite solar cells. *J. Phys. Chem. Lett.* **6**, 3923-3930 (2015).

15. Pockett, A. et al. Characterization of planar lead halide perovskite solar cells by impedance spectroscopy, open-circuit photovoltage decay, and intensity-modulated photovoltage/photocurrent spectroscopy. *J. Phys. Chem. C* **119**, 3456-3465 (2015).

16. Hailegnaw, B., Sariciftci, N. S. & Scharber, M. C. Impedance spectroscopy of perovskite solar cells: studying the dynamics of charge carriers before and after continuous operation. *Phys. Status Solidi A* **217**, 2000291 (2020).

17. Riquelme, A., Gálvez, F. E., Contreras-Bernal, L., Míguez, H. & Anta, J. A. Internal quantum efficiency and time signals from intensity-modulated photocurrent spectra of perovskite solar cells. *J. Appl. Phys.* **128**, 133103 (2020).

18. Almora, O., García-Batlle, M. & Garcia-Belmonte G. Utilization of temperature-sweeping capacitive techniques to evaluate band gap defect densities in photovoltaic

perovskites. *J. Phys. Chem. Lett.* **10**, 3661-3669 (2019).

19.   Bisquert, J. & Janssen, M. From frequency domain to time transient methods for halide perovskite solar cells: the connections of IMPS, IMVS, TPC, and TPV. *J. Phys. Chem. Lett.* **12**, 7964-7971 (2021).

20.   Ponomarev, E. & Peter, L. A generalized theory of intensity modulated photocurrent spectroscopy (IMPS). *J. Electroanal. Chem.* **396**, 219-226 (1995).

21.   Guillén, E., Ramos, F. J., Anta, J. A. & Ahmad S. Elucidating transport-recombination mechanisms in perovskite solar cells by small-perturbation techniques. *J. Phys. Chem. C* **118**, 22913-22922 (2014).

22.   Zarazua, I. et al. Surface recombination and collection efficiency in perovskite solar cells from impedance analysis. *J. Phys. Chem. Lett.* **7**, 5105-5113 (2016).

23.   Su, L., Méndez, M., Jiménez-López, J., Zhu, M., Xiao, Y. & Gil E. J. P. Analysis of the oxygen passivation effects on $MAPbI_3$ and $MAPbBr_3$ in fresh and aged solar cells by the transient photovoltage technique. *ChemPlusChem* **86**, 1316-1321 (2021).

24.   McNeill, C. R., Hwang, I. & Greenham, N. C. Photocurrent transients in all-polymer solar cells: trapping and detrapping effects. *J. Appl. Phys.* **106**, 024507 (2009).

25.   Neukom, M., Züfle, S., Jenatsch, S. & Ruhstaller, B. Opto-electronic characterization of third-generation solar cells. *Sci. Technol. Adv. Mater.* **19**, 291-316 (2018).

26.   Ravishankar, S., Liu, Z., Wang, Y., Kirchartz, T. & Rau, U. How charge carrier exchange between absorber and contact influences time constants in the frequency domain response of perovskite solar cells. *arXiv preprint arXiv:230309908*, (2023).

27.   Futscher, M. H. et al. Quantification of ion migration in $CH_3NH_3PbI_3$ perovskite solar cells by transient capacitance measurements. *Mater. Horiz.* **6**, 1497-1503 (2019).

28.   Awni, R. A. et al. Influence of charge transport layers on capacitance measured in halide perovskite solar cells. *Joule* **4**, 644-657 (2020).

29.   Shockley, W. & Read Jr, W. Statistics of the recombinations of holes and electrons. *Phys. Rev.* **87**, 835 (1952).

30.   Azzouzi, M. et al. Overcoming the limitations of transient photovoltage measurements for studying recombination in organic solar cells. *Sol. RRL* **4**, 1900581 (2020).

31.   Herz, L. M. Charge-carrier mobilities in metal halide perovskites: fundamental mechanisms and limits. *ACS Energy Lett.* **2**, 1539-1548 (2017).

32.   Stavrakas, C. et al. Visualizing buried local carrier diffusion in halide perovskite crystals via two-photon microscopy. *ACS Energy Lett.* **5**, 117-123 (2020).

33.   Cardenas-Morcoso, D., Bou, A., Ravishankar, S., García-Tecedor, M., Gimenez, S. & Bisquert, J. Intensity-modulated photocurrent spectroscopy for solar energy conversion devices: what does a negative value mean? *ACS Energy Lett.* **5**, 187-191 (2020).

34.   Pockett, A., Spence, M., Thomas, S. K., Raptis, D., Watson, T. & Carnie, M. J. Beyond the first quadrant: origin of the high frequency intensity-modulated photocurrent/photovoltage spectroscopy response of perovskite solar cells. *Sol. RRL* **5**, 2100159 (2021).

35.   Wang, H., Guerrero, A., Bou, A., Al-Mayouf, A. M. & Bisquert, J. Kinetic and material
16

properties of interfaces governing slow response and long timescale phenomena in perovskite solar cells. *Energy Environ. Sci.* **12**, 2054-2079 (2019).

36. Cai, M. et al. Control of electrical potential distribution for high-performance perovskite solar cells. *Joule* **2**, 296-306 (2018).

37. Sandberg, O. J. et al. On the question of the need for a built-In potential in perovskite solar cells. *Adv. Mater. Interfaces* **7**, 2000041 (2020).

38. Bisquert, J. Chemical capacitance of nanostructured semiconductors: its origin and significance for nanocomposite solar cells. *Phys. Chem. Chem. Phys.* **5**, 5360-5364 (2003).

39. Krückemeier, L., Krogmeier, B., Liu, Z., Rau, U. & Kirchartz, T. Understanding transient photoluminescence in halide perovskite layer stacks and solar cells. *Adv. Energy Mater.* **11**, 2003489 (2021).

40. Krückemeier, L., Liu, Z., Krogmeier, B., Rau, U. & Kirchartz, T. Consistent interpretation of electrical and optical transients in halide perovskite layers and solar cells. *Adv. Energy Mater.* **11**, 2102290 (2021).

41. Rau, U., Huhn, V. & Pieters, B. E. Luminescence analysis of charge-carrier separation and internal series-resistance losses in Cu(In, Ga)Se$_2$ solar cells. *Phys. Rev. Appl.* **14**, 014046 (2020).

17

Supplementary Files

This is a list of supplementary files associated with this preprint. Click to download.

- 230524risetimefrequencydomainpaperSI.docx